

# Spin-orbit coupled correlated metal phase in Kondo lattices: an implementation with alkaline-earth atoms

L. Isaev, J. Schachenmayer, and A. M. Rey  
 JILA, NIST, Department of Physics & Center for Theory of Quantum Matter,  
 University of Colorado, 440 UCB, Boulder, CO 80309, USA

We show that an interplay between quantum effects, strong on-site ferromagnetic exchange interaction and antiferromagnetic correlations in Kondo lattices can give rise to an exotic spin-orbit coupled metallic state in regimes where classical treatments predict a trivial insulating behavior. This phenomenon can be simulated with ultracold alkaline-earth fermionic atoms subject to a laser-induced magnetic field by observing dynamics of spin-charge excitations in quench experiments.

PACS numbers: 72.15.-v, 75.20.Hr, 67.85.-d, 37.10.Jk

*Introduction.*— The behavior of correlated quantum systems can rarely be understood in terms of individual atoms or electrons, and instead is determined by a competition between their strong interactions and kinetic energy [1]. This interplay often places states with fundamentally different properties energetically close to each other, and hence makes the system highly sensitive to external controls such as pressure, or magnetic field [2].

A paramount example of correlation-driven tunable phenomena is the colossal magneto-resistance in transition-metal oxides, e.g. manganites [3, 4]. Properties of these materials are governed by the ferromagnetic Kondo lattice model (FKLM) which includes competition between kinetic energy of itinerant electrons and their Hund exchange coupling with localized spins [5, 6]. This interaction often exceeds the conduction bandwidth and ensures that only on-site triplets, i.e. electrons whose spins are aligned with local magnetic moments, can exist at low energy. For classical core spins ( $S \gg 1$ ), an effective electron hopping amplitude between two lattice sites strongly depends on the magnetic background: it is largest when local spins on the two sites are parallel, and vanishes for anti-parallel [antiferromagnetically (AF) ordered] local moments [7, 8]. As a result, the conductivity of a system becomes highly sensitive to small variations in the magnetic texture, e.g. caused by an external magnetic field. This so-called double-exchange (DE) physical picture remains qualitatively valid when quantum fluctuations of the local magnetism are taken into account [9–13] and in the extreme quantum case  $S = \frac{1}{2}$  [14].

Nevertheless, even early works [8] hinted at a breakdown of the DE semiclassical description in the presence of strong AF correlations between local spins when they form at least short-range Néel order. While in an ideal antiferromagnet an electron can not move, it still gains energy via smooth deformations of the Néel background [8]. Quantum fluctuations would allow local spins to form singlets with mobile fermions and further distort the AF texture. Even for Hund coupling comparable to the conduction bandwidth these processes are important and can lead to an increase of the electron effective mass [15].

In the present Letter we demonstrate that quantum nature of the local magnetism *dramatically affects* physics of a FM Kondo lattice with AF correlations between core spins [Fig. 1(a)]. We focus on a  $S = \frac{1}{2}$  FKLM in the strong-coupling regime, when Hund and AF interactions exceed the electron bandwidth, and show that the AF environment of each core moment frustrates the on-site Hund exchange  $V$  [Fig. 1(b)]. Properties of the model are controlled by a competition between  $V$  and an energy scale  $\Omega$  of the antiferromagnetism. When these energies are significantly different, the system is an insulator with localized band electrons. However, near the resonance  $V \approx \Omega$ , the AF and Hund interactions effectively cancel each other allowing quantum effects to stabilize a new *correlated metal* phase whose quasiparticles admix singlet and triplets states of bare electrons and local spins. These excitations distort the AF order and give rise to a *transverse* (to the Néel vector) magnetization. This resonant behavior is absent in a semiclassical DE theory which predicts an insulating state for any Hund coupling.

The correlated metal phase can be observed in fermionic alkaline-earth atoms (AEAs) [16], such as  $^{87}\text{Sr}$  [17] or  $^{173}\text{Yb}$  [18–23], in a two-band optical lattice where atoms in the lowest (localized) and higher (itinerant) bands correspond to core spins and mobile fermions, respectively [Fig. 1(c)]. We propose to simulate the AF background with an artificial, laser-induced magnetic field [24–26], which in AEAs can be implemented either using Raman transitions between nuclear spin levels [27] or Rabi coupling of  $^1S_0$  and  $^3P_0$  electronic clock states [28]. The laser phase can be controlled to vary from one lattice site to the next in a *staggered* fashion, while the Rabi or Raman coupling of relevant atomic states provides a handle of the above singlet-triplet (s-t) resonance.

*Correlated metal in a strongly-coupled FKLM.*— Let us consider a generic FM Kondo lattice with AF superexchange interactions between core moments:

$$H = -J_0 \sum_{\langle ij \rangle} (c_{in}^\dagger c_{jn} + \text{h.c.}) + I_H \sum_{\langle ij \rangle} S_i^z S_j^z - V \sum_i [\mathbf{S}_i^\perp \cdot \mathbf{s}_{ci}^\perp + \eta S_i^z s_{ci}^z] + R \sum_{\langle ij \rangle} n_i^c n_j^c, \quad (1)$$

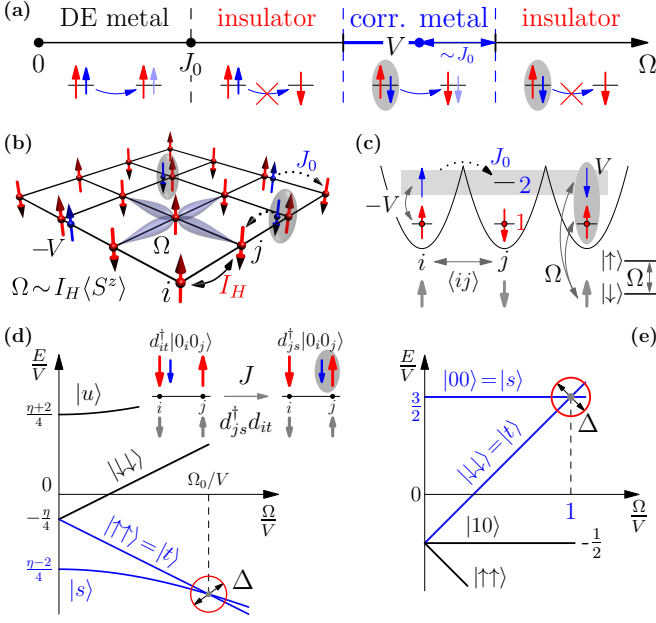


FIG. 1. (a) Schematic phase diagram of Eq. (1) with  $V \gg J_0$  ( $\Omega$  is the AF interaction strength), featuring the correlated metal state for strong coupling  $\Omega \sim V$ . The conventional ferromagnetic (DE) metal occurs at  $\Omega \lesssim J_0$ . Bottom row: allowed and forbidden (indicated by red crosses) hopping processes. Blue (red) color marks mobile (local) fermions. Light blue spins show final states of itinerant fermions. Gray ellipses denote local entangled singlet-triplet (s-t) states [ $|s\rangle$  in (d)]. (b) The electronic model of Eq. (1). Color notations are as in (a). Local spins feel a staggered mean-field  $\Omega \sim I_H \langle S^z \rangle$  due to the AF background. (c) Optical lattice of the AEA setup Eq. (5). Band 1 (2) is localized (itinerant). Gray arrows indicate the laser-induced staggered Zeeman field  $\Omega$  that splits pseudo-spin  $|\uparrow, \downarrow\rangle$  states. Gray ellipse is a spin-singlet state. Other notations are as in (b). (d) Energies on an isolated site with one fermion. Blue lines [red circle] indicate the s-t subspace [resonance]. Inset: Hopping of s-t excitations  $d_{i\alpha}^\dagger$  (3). Other notations are as in (a). (e) Same as in (d), but for the AEA model (5). The s-t subspace is an excited manifold.

defined on a bipartite (e.g. square) lattice of Fig. 1(b). Here  $c_{in}^\dagger$  creates an electron with spin  $n = \uparrow, \downarrow$  (we assume summation over repeated indices) at site  $i = 1 \dots N$ . The first line contains nearest-neighbor (NN) hopping  $J_0$  on a link  $\langle ij \rangle$ , and the AF exchange  $I_H > 0$  between local moments  $\mathbf{S}_i$ . The latter are coupled to mobile spins  $\mathbf{s}_{ci} = \frac{1}{2} c_{in}^\dagger \boldsymbol{\sigma}_{nm} c_{im}$  ( $\boldsymbol{\sigma}$  are Pauli matrices) via a FM Hund exchange  $V$  with an  $XXZ$  anisotropy ( $\perp$  denotes  $xy$  vector components)  $\eta \in [0, 1]$  arising from atomic spin-orbit coupling and crystal-field effects. Due to same reasons, the AF interaction is also anisotropic: we consider the simplest Ising limit, but our results are applicable to a general  $XXZ$  case. The last term (with  $n_{ci}^c = c_{in}^\dagger c_{in}$ ) is a NN Coulomb repulsion (see below).

We focus on the strong-coupling limit  $J_0 \ll I_H, V$  and assume that core moments are AF-ordered,  $\langle S_i^z \rangle =$

$\langle S^z \rangle e^{i\mathbf{Q} \cdot \mathbf{x}_j}$  [ $\mathbf{x}_j \equiv j$ ,  $\mathbf{Q} = \pi$  for a one- (1D),  $(\pi, \pi)$  for a two-dimensional (2D) lattice, etc]. Mobile electrons will form entangled states with local spins, and above certain density  $n^c > n_{cr}^c$ , destroy the Néel order even for  $J_0 \equiv 0$ . Hence, the above assumption is valid only in the low-density regime  $n^c \ll 1$  when electrons rarely occupy NN sites. This regime is enforced by the repulsion  $R$  in Eq. (1). The AF background can be taken into account by performing a staggered transformation:

$$c_{in} = a_{in} \quad (i \text{ even}); \quad c_{in} = a_{i,-n} \quad (i \text{ odd});$$

$$\mathbf{S}_i = (T_i^x, (-1)^i T_i^y, (-1)^i T_i^z), \quad (2)$$

where  $a_{in}$  and  $\mathbf{T}_i$  are new mobile fermions and local spins. As a result, the first line in Eq. (1) becomes  $-\sum_{\langle ij \rangle} [J_0 \sigma_{nm}^x (a_{in}^\dagger a_{jm} + \text{h.c.}) + I_H T_i^z T_j^z]$ ; other terms remain unchanged with  $c_{in} \rightarrow a_{in}$  ( $\mathbf{s}_{ci} \rightarrow \mathbf{s}_{ai}$ ) and  $\mathbf{S}_i \rightarrow \mathbf{T}_i$ .

In this staggered frame, the mean-field Hamiltonian of an isolated site is  $H_i = -V[\mathbf{T}_i^\perp \cdot \mathbf{s}_{ai}^\perp + \eta T_i^z s_{ai}^z] - z I_H \langle T_j^z \rangle T_i^z$ . Here the last term is a molecular field acting on a core spin in the AF environment and  $z$  is the lattice coordination number. We assume that  $\langle T_j^z \rangle = \langle T^z \rangle > 0$  is  $j$ -independent and denote  $\Omega = z I_H \langle T^z \rangle$ . In a low-density regime, we can focus only on the  $n_i^a = 1$  subspace [see Fig. 1(d)]. There are two states with total spin projection  $T_t^z = \pm 1$ :  $|t\rangle_i = a_{i\uparrow}^\dagger |\uparrow\rangle_i$  and  $|\downarrow\rangle_i = a_{i\downarrow}^\dagger |\downarrow\rangle_i$  and energies  $E_{1,2} = -\frac{\eta}{4}V \mp \frac{1}{2}\Omega$ ; and two  $T_t^z = 0$  states:  $|u, s\rangle_i = r_\pm a_{i\uparrow}^\dagger |\downarrow\rangle_i \mp r_\mp a_{i\downarrow}^\dagger |\uparrow\rangle_i$  with energies  $E_{u,s} = \frac{\eta}{4}V \pm \frac{1}{2}\sqrt{V^2 + \Omega^2}$ , where  $|n\rangle$  is a core-spin state,  $r_\pm = \frac{1}{\sqrt{2}}(\cos \vartheta \pm \sin \vartheta)$ ,  $\tan 2\vartheta = \Omega/V$  (here  $|\sigma\rangle_i$  is a shorthand notation for  $|\sigma\rangle_i \otimes |0\rangle$ ,  $|0\rangle$  is the  $a$ -fermion vacuum). When  $\Omega = \Omega_0 = (1 - \eta^2)V/2\eta$ ,  $|s\rangle_i$  and  $|t\rangle_i$  become degenerate, and at strong-coupling define the local s-t subspace. For  $\Omega \sim \Omega_0$  other states, separated by a large gap  $\sim \Omega_0$ , can be ignored. We represent this Hilbert space with *constrained (no double occupancy) fermions* [29]

$$d_{is}^\dagger |\text{vac}\rangle \leftrightarrow |s\rangle_i, \quad d_{it}^\dagger |\text{vac}\rangle \leftrightarrow |t\rangle_i. \quad (3)$$

Here  $|\text{vac}\rangle = \prod_i |\uparrow\rangle_i$  is a vacuum state with  $n_i^a = 0$ .

Near the resonance  $\Omega = \Omega_0$ , the system is described by an effective Dirac-like Hamiltonian

$$H_d = -J \sum_{\langle ij \rangle} [\sigma_{\alpha\beta}^x d_{i\alpha}^\dagger d_{j\beta} + \text{h.c.}] + \Delta \sum_i (n_{is}^d - n_{it}^d), \quad (4)$$

obtained by projecting the Hamiltonian (1) onto s-t subspace (3), i.e. by computing matrix elements of Eq. (1) between states  $d_{i\alpha}^\dagger |\text{vac}\rangle$  [30]. In Eq. (4),  $J = J_0 r_+$ ,  $\alpha, \beta = s$  or  $t$ , and  $n_{i\alpha}^d = d_{i\alpha}^\dagger d_{i\alpha}$  (with  $n_i^d = n_{is}^d + n_{it}^d$ ). The first term contains hopping processes [see inset in Fig. 1(d)] that mix local entangled  $|s\rangle$  and classical  $|t\rangle$  states (3) [because of  $\sigma_{\alpha\beta}^x$ ]. This emergent spin-orbit coupling is rooted in an interplay between strong exchange interactions and quantum fluctuations, and manifests in a *transverse* [orthogonal to Néel vector  $\langle S_i^z \rangle$ ] spin polarization of

$d$ -particles:  $\mathbf{T}_i^\perp = \frac{r_\pm}{r_-} \mathbf{s}_{ai}^\perp = \frac{1}{2} r_+ \boldsymbol{\sigma}_{\alpha\beta}^\perp d_{i\alpha}^\dagger d_{i\beta}$ . The second term contains an effective detuning  $\Delta = \Omega - \Omega_0$  from the s-t resonance and describes a competition between Hund interaction and AF correlations, both favoring an insulator (at large  $|\Delta| \gg J$ ) with localized fermions. Remarkably, for  $|\Delta| \sim J$  the state of the system is driven by a subdominant kinetic-energy scale  $J$ , which stabilizes a *correlated metallic phase* of  $d$ -fermions with transverse spin excitations. Within the low-energy model (4), the sign of  $\Delta$  is irrelevant because under a canonical transformation  $d_{i\alpha} \rightarrow \sigma_{\alpha\beta}^x d_{i\beta}$ ,  $H_d(-\Delta) \rightarrow H_d(\Delta)$ . Hence, below we assume that  $\Delta \geq 0$ .

The s-t resonance occurs because  $\eta < 1$ . In the isotropic ( $\eta = 1$ ) strong-coupling case Eq. (1) describes an insulator with localized triplets (similar to a DE model [7]). However, this state is unstable for  $\eta < 1$  and  $I_H \sim V$ . The existence of a s-t resonance does not contradict the “poor man” scaling [31, 32] where the  $XY$  exchange  $V$  flows to zero at low energies. Indeed, the latter is applicable only at weak coupling  $V \ll J_0$ , while our theory operates in the opposite, *strong coupling regime*  $V \gg J_0$ .

*Singlet-triplet resonance with AEAs.*— The correlated metal phase may be challenging to observe in a solid-state system due to a multitude of parameters in Eq. (1) that need to be tuned near the s-t resonance. Here we propose to realize this phase using two-level AEAs in an optical lattice of Fig. 1(c). The spin- $\frac{1}{2}$  degrees of freedom can be implemented using either (i) nuclear spins of atoms in the  $|g\rangle$  electronic state, or (ii)  $|e, g\rangle$  clock states of nuclear-spin polarized atoms. The Hamiltonian of the system is:

$$H = -J_0 \sum_{\langle ij \rangle} (c_{i2n}^\dagger c_{j2n} + \text{h.c.}) - \sum_i [V c_{i1n}^\dagger c_{i1m} c_{i2m}^\dagger c_{i2n} + \Omega(-1)^i (c_{ia\uparrow}^\dagger c_{ia\uparrow} - c_{ia\downarrow}^\dagger c_{ia\downarrow})] + U \sum_i n_{i2\uparrow}^c n_{i2\downarrow}^c, \quad (5)$$

where  $c_{ian}^\dagger$  creates a fermion at site  $i$  in Bloch band  $a = 1, 2$  with spin  $n$ . Band 1 is localized and contains one atom per site, while the itinerant band 2 has an arbitrary filling and a NN hopping  $J_0$  [33]. The second term in Eq. (5) is an interband exchange interaction. It is FM ( $V > 0$ ) because atoms can experience  $s$ -wave collisions only in a spin-singlet state. The third term contains the *staggered* [indicated by  $(-1)^i = e^{i\mathbf{Q} \cdot \mathbf{x}_i}$ ] Zeeman-like Raman [in case (i)] or direct Rabi [for case (ii)] coupling, with  $\Omega > 0$  which simulates the AF environment in Fig. 1(b) [34]. Finally, there is a local repulsion  $U$  due to intraband  $s$ -wave collisions ( $n_{ian}^c = c_{ian}^\dagger c_{ian}$ ).

Since atoms in band 1 are localized they only contribute spin degrees of freedom,  $\mathbf{S}_i = \frac{1}{2} \boldsymbol{\sigma}_{nm} c_{i1n}^\dagger c_{i1m}$ . Up to a density-density interaction, magnetic terms in Eq. (5) can be rewritten as  $-2 \sum_i [V \mathbf{S}_i \cdot \mathbf{s}_{ci} + \Omega(-1)^i (S_i^z + s_{ci}^z)]$ , where we omitted the band index,  $c_{in} \equiv c_{i2n}$ . Applying the transformation (2) to Eq. (5), we get rid of  $(-1)^i$ , and replace  $c_{in} \rightarrow a_{in}$  ( $\mathbf{s}_{ci} \rightarrow \mathbf{s}_{ai}$ ) and  $\mathbf{S}_i \rightarrow \mathbf{T}_i$ .

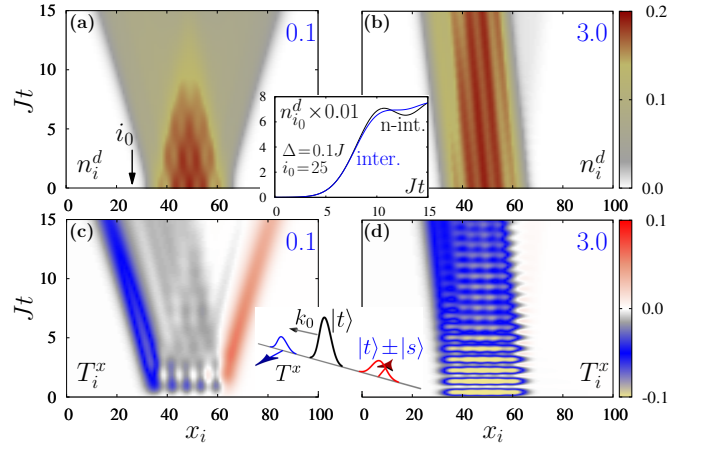


FIG. 2. Propagation of wavepackets with 5 particles. (a) and (b) show total density  $\langle n_i^d(t) \rangle$ ; (c) and (d) contain the transverse local-spin polarization  $\langle T_i^x \rangle$ . Blue numbers in top right corners indicate the detuning  $\Delta/J$ . Inset: comparison between density evolution at a fixed  $x_i = i_0$  [black arrow in panel (a)] in the full model (4) (blue line) and in the case of non-interacting (n-int)  $d$ -fermions (black line). The parameters are  $N = 101$ ,  $A = 10^{-3}J$ , and  $k_0 = -20\pi/N$ .

On an isolated site  $i$  there are 8 eigenvalues  $E_{n^a}(T_t, T_t^z)$  labeled by the total spin  $T_t$ , its projection  $T_t^z$  and fermion number  $n^a$ :  $E_0(\frac{1}{2}, \pm\frac{1}{2}) = E_2(\frac{1}{2}, \pm\frac{1}{2}) - U = \mp\Omega$ ,  $E_1(0, 0) = -3E_1(1, 0) = \frac{3}{2}V$  and  $E_1(1, \pm 1) = -\frac{V}{2} \mp 2\Omega$ . Energy levels with  $n^a = 1$  are shown in Fig. 1(e). For small  $J_0$  a mobile atom can propagate only when two or more states are at resonance, i.e. for  $\Omega = 0$  or  $V$ . The first case is a usual FKLm [5] without AF correlations.

We will concentrate on the second resonance at  $\Omega = V$ , reached in an *excited* s-t manifold spanned by the local singlet  $|s\rangle_i = \frac{1}{\sqrt{2}}[a_{i\uparrow}^\dagger|\downarrow\rangle_i - a_{i\downarrow}^\dagger|\uparrow\rangle_i]$  and triplet  $|t\rangle_i = a_{i\downarrow}^\dagger|\downarrow\rangle_i$  [red circle in Fig. 1(e)], and identify these states with the corresponding states (3): now  $d_{is}^\dagger$  creates a pure spin-singlet, while  $d_{it}^\dagger$  creates a triplet. In an excited manifold, the vacuum state  $|\text{vac}\rangle = \prod_i |\downarrow\rangle_i$  has local spins *antiparallel* to  $\Omega$ . Near the s-t resonance, other singly-occupied states are separated by a gap  $\sim V$  and can be ignored, together with the doubly-occupied manifold. The system is described by the effective model (4) with  $J = \frac{1}{\sqrt{2}}J_0$ ,  $\Delta = V - \Omega$  [35]. Thus, in a strong-coupling regime  $J_0 \ll \Omega, V$  and for  $\Omega \sim V$ , the AEA setup (5) can be used to simulate the s-t resonance dynamics of Eq. (1). For example, the transverse magnetization of a  $d$ -particle is now  $\mathbf{T}_i^\perp = -\mathbf{s}_{ai}^\perp = -\boldsymbol{\sigma}_{\alpha\beta}^\perp d_{i\alpha}^\dagger d_{i\beta}/\sqrt{8}$ . We focus on the excited s-t manifold because a cold-atom system is usually well-isolated from its environment and can not escape the s-t subspace due to decoherence.

*Wavepacket dynamics in 1D.*— The spin-motion coupling and transverse spin of  $d$ -fermions can be probed via propagation of many-body wavepackets. We focus on

a 1D case and study dynamics of the model (4) within a time-dependent density matrix renormalization group (t-DMRG) method [36–39]. The initial wavefunction is assumed to contain only triplets and is a ground state (GS) of the Hamiltonian  $H_{1D}(t < 0) = -J \sum_i [d_{it}^\dagger d_{i+1,t} + \text{h.c.}] + A \sum_i [x_i - \frac{N}{2}]^2 n_{it}^d$  that describes fermions  $d_{it}$  in a harmonic trap with  $A > 0$ . At  $t = 0$ , the trap is removed, so  $H_{1D}(t \geq 0) = H_d$ , and the packet is accelerated to a momentum  $k_0$  by applying an operator  $e^{ik_0 \sum_i x_i n_{it}^d}$ .

Fig. 2 shows evolution of five-fermion wavepackets for  $\Delta = 0.1J$  and  $\Delta = 3J$ . Near the s-t resonance, the initial distribution splits into two fast counter-propagating parts with *opposite* transverse local magnetization  $\langle T_i^x \rangle$  [Fig. 2(a) and (c)], while for large  $\Delta$  this splitting is negligible and the state remains practically localized [Fig. 2(b) and (d)]. To understand this behavior, we consider dynamics of a single  $d$ -fermion, when the Hamiltonian (4) can be diagonalized in terms of quasiparticles with dispersion  $\varepsilon_{k\lambda} = \lambda \rho_k = \lambda \sqrt{(2J \cos k)^2 + \Delta^2}$  ( $\lambda = \pm$ ) [40]. Because these bands have opposite group velocities  $v_{k\lambda}^\pm = \lambda \partial_k \rho_k$ , after a time  $t > 1/J$  the density has an approximate form  $\langle n_{i\alpha}^d(t) \rangle \approx R_\alpha(\xi_-) + L_\alpha(\xi_+)$  where  $\xi_\pm = x_i \pm v_{k_0}^- t$ ,  $v_{k_0}^- = -2J |\sin k_0| / \rho_{k_0}$ , and  $L_\alpha$ ,  $R_\alpha$  with  $\frac{R_s}{L_s} \approx 1$  and  $\frac{R_t}{L_t} \approx (\frac{\rho_{k_0} - \Delta}{\rho_{k_0} + \Delta})^2$  describe right and left movers. For large  $\Delta$ ,  $R_t \ll L_t$  [see Fig. 2(b)],  $\langle T_i^x(Jt > 1) \rangle \approx R(\xi_-) + L(\xi_+)$ , with  $\frac{R}{L} \approx -\frac{\rho_{k_0} - \Delta}{\rho_{k_0} + \Delta} < 0$  [Fig. 2(c)]. This single-particle picture is valid near wavepacket edges with low fermion density [see inset of Fig. 2], and breaks down at the strongly-correlated core.

*The correlated metallic state.*— To capture interaction effects that lead to correlated metal phase and drive metal-insulator transitions, in Fig. 3 we compute phase diagram of Eq. (4) in 1D, as a function of the detuning  $\Delta$  and chemical potential  $\mu$  (described by a term  $\delta H_d = -\mu \sum_i n_i^d$ ). We characterize various GSs with a Drude weight (DW)  $\mathcal{D}$  related to the longitudinal conductivity as  $\text{Re } \sigma_{xx}(\omega \rightarrow 0) = \mathcal{D} \delta(\omega)$ :  $\mathcal{D} > 0$  for a metal and vanishes in an insulator. For a system with periodic boundary conditions,  $\mathcal{D} = \frac{1}{N} \frac{d^2 \mathcal{E}_0}{d\phi^2} \big|_{\phi=0}$  where  $\mathcal{E}_0$  is the GS energy and  $\phi N$  is the flux piercing the ring [41, 42]. In Eq. (4) we replace  $d_{i\alpha}^\dagger d_{i+1,\beta} \rightarrow d_{i\alpha}^\dagger e^{i\phi} d_{i+1,\beta}$  and treat this model using an unbiased DMRG technique [43].

The physics of a non-interacting (n-int) model (4) is determined by filling of single-particle bands  $\varepsilon_{k\lambda}$ : When  $\mu$  is inside one of them the system is a metal (regions below dashed red line in Fig. 3), otherwise it is a band insulator [44]. The correlated nature of  $d$ -fermions qualitatively changes this picture by dramatically suppressing the metallic phase and transforming the band insulator to either *charge density-wave* (CDW) with  $n^d < 1$ , or a *triplet Mott state* with  $n^d = n_t^d = 1$ . Metallic, CDW and Mott phases are separated by a 1st order transition. Surprisingly, a CDW state with  $n^d = 0.5$  emerges exactly at  $\mu = -\Delta$ , right at the metal-insulator transition

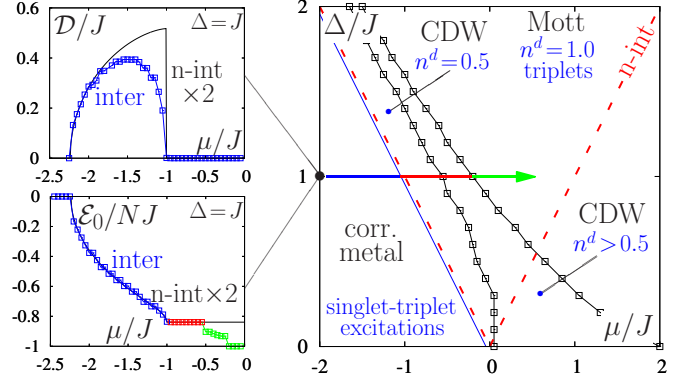


FIG. 3. Phase diagram of the model (4) on a  $N = 40$  site chain with periodic boundary conditions. Black and blue lines mark 1st order transitions. For the correlated metal phase, the Drude weight  $\mathcal{D} > 0$ , while in all other states  $\mathcal{D} = 0$ . Dashed red line separates metallic (below) and band insulator (above) states in a model with non-interacting (n-int)  $d$ -fermions. At  $\Delta = 0$ ,  $\mathcal{D} = \frac{1}{\pi} \sqrt{(2J)^2 - \mu^2}$  for  $|\mu| < 2J$  and 0 otherwise. On the left: Drude weight and ground-state energy  $\mathcal{E}_0$  for  $\Delta = J$  plotted along the arrow in the main panel. Notations are as in Fig. 2. Notice jumps in  $\frac{\partial \mathcal{E}_0}{\partial \mu}$  at phase transitions. For  $\mu \approx -0.5$  (CDW state),  $\mathcal{E}_0$  decreases with increasing  $n_t^d$ . For n-int fermions, one has to multiply  $\mathcal{D}$  and  $\mathcal{E}_0$  (black curves) by 2 due to spin degeneracy, absent for constrained  $d$ -fermions.

for non-interacting fermions. While the latter is driven by a simple band filling, the CDW arises due to quantum effects: For  $\mu = -\Delta$  the on-site energy of a triplet vanishes which results in a macroscopic degeneracy (associated with different fillings of triplets) of the classical GS. Quantum fluctuations due to s-t virtual hoppings then select a GS with a two-site unit cell. For  $n^d > 0.5$  this state evolves into CDWs with larger unit cells.

At low density, one can extract the DW from a group velocity of a wavepacket with small momentum  $k_0$ ,  $v_{k_0}^- \approx \frac{k_0}{m^*} [m^* = \frac{1}{(2J)^2} \sqrt{(2J)^2 + \Delta^2}]$ , as  $\mathcal{D}(n^d \ll 1) \approx \frac{n^d}{m^*} = \frac{n^d v_{k_0}^-}{k_0}$ .

*Discussion.*— The state of a many-body system with competing strong interactions often has unexpected physical properties and is driven by a subdominant energy scale. We illustrated this mechanism in a FKLM where an interplay between strong on-site FM exchange and AF correlations, each favoring an insulating behavior, allows the small kinetic energy to stabilize a correlated *metallic* phase, whose elementary excitations involve resonating singlet and triplet states of bare local spins and mobile fermions. This s-t mixing leads to a distortion of the AF order and local magnetization *perpendicular* to the Néel vector. We also showed how one can probe this physics in a quantum simulator with AEAs in optical lattices under a laser-induced magnetic field.

Our results, obtained using a low-energy model (4), remain valid within the full Hamiltonian (5) with  $\Omega > J$

[45], and should be applicable beyond 1D, because the phases in Fig. 3 are not associated with spontaneous breaking of any continuous symmetry.

The observation of wavepacket dynamics in Fig. 2 and transverse spin excitations does not require temperatures  $\sim J$  and relies on an uncorrelated initial triplet state. These features can be probed in quench experiments with AEAs in moving optical lattices [46]. The Drude weight  $\mathcal{D}$  can be measured as a response to a weak optical lattice tilt [47]. Thus the phase diagram in Fig. 3 can be verified, at least for low-densities and deep lattices when the band relaxation due to collisions is energetically suppressed.

*Acknowledgments.*— We thank Ivar Martin for illuminating discussions. This work was supported by NSF (PHY-1211914, PHY-1521080 and PFC-1125844), AFOSR FA9550-13-1-0086, AFOSR-MURI Advanced Quantum Materials, NIST and ARO W911NF-12-1-0228 individual investigator awards.

- 
- [1] P. W. Anderson, *Science* **177**, 393 (1972).
  - [2] E. Morosan, D. Natelson, A. H. Nevidomskyy, and Q. Si, *Adv. Mater.* **24**, 4896 (2012).
  - [3] E. Dagotto, *Science* **309**, 257 (2005).
  - [4] E. Dagotto, *New Journal of Physics* **7**, 67 (2005).
  - [5] Y. A. Izyumov and Y. N. Skryabin, *Physics-Uspokhi* **44**, 109 (2001).
  - [6] D. M. Edwards, *Advances in Physics* **51**, 1259 (2002).
  - [7] P. W. Anderson and H. Hasegawa, *Phys. Rev.* **100**, 675 (1955).
  - [8] P. G. de Gennes, *Phys. Rev.* **118**, 141 (1960).
  - [9] E. Müller-Hartmann and E. Dagotto, *Phys. Rev. B* **54**, R6819 (1996).
  - [10] J. Zang, H. Rder, A. R. Bishop, and S. A. Trugman, *Journal of Physics: Condensed Matter* **9**, L157 (1997).
  - [11] R. E. Brunton and D. M. Edwards, *Journal of Physics: Condensed Matter* **10**, 5421 (1998).
  - [12] E. Dagotto, S. Yunoki, A. L. Malvezzi, A. Moreo, J. Hu, S. Capponi, D. Poilblanc, and N. Furukawa, *Phys. Rev. B* **58**, 6414 (1998).
  - [13] N. Shannon and A. V. Chubukov, *Phys. Rev. B* **65**, 104418 (2002).
  - [14] J. Kienert and W. Nolting, *Phys. Rev. B* **73**, 224405 (2006).
  - [15] K. Le Hur, *Phys. Rev. B* **75**, 014435 (2007).
  - [16] A. V. Gorshkov, M. Hermele, V. Gurarie, C. Xu, P. S. Julienne, J. Ye, P. Zoller, E. Demler, M. D. Lukin, and A. M. Rey, *Nat. Phys.* **6**, 289 (2010).
  - [17] X. Zhang, M. Bishof, S. L. Bromley, C. V. Kraus, M. S. Safronova, P. Zoller, A. M. Rey, and J. Ye, *Science* **345**, 1467 (2014).
  - [18] G. Cappellini, M. Mancini, G. Pagano, P. Lombardi, L. Livi, M. Siciliani de Cumis, P. Cancio, M. Pizzocaro, D. Calonico, F. Levi, C. Sias, J. Catani, M. Inguscio, and L. Fallani, *Phys. Rev. Lett.* **113**, 120402 (2014).
  - [19] F. Scazza, C. Hofrichter, M. Höfer, P. C. De Groot, I. Bloch, and S. Fölling, *Nat. Phys.* **10**, 779 (2014).
  - [20] G. Pagano, M. Mancini, G. Cappellini, L. Livi, C. Sias, J. Catani, M. Inguscio, and L. Fallani, *Phys. Rev. Lett.* **115**, 265301 (2015).
  - [21] M. Höfer, L. Riegger, F. Scazza, C. Hofrichter, D. R. Fernandes, M. M. Parish, J. Levinsen, I. Bloch, and S. Fölling, *Phys. Rev. Lett.* **115**, 265302 (2015).
  - [22] R. Zhang, Y. Cheng, H. Zhai, and P. Zhang, *Phys. Rev. Lett.* **115**, 135301 (2015).
  - [23] R. Zhang, D. Zhang, Y. Cheng, W. Chen, and H. Z. Peng Zhang, arXiv:1509.01350.
  - [24] J. Dalibard, F. Gerbier, G. Juzeliūnas, and P. Öhberg, *Rev. Mod. Phys.* **83**, 1523 (2011).
  - [25] A. Celi, P. Massignan, J. Ruseckas, N. Goldman, I. B. Spielman, G. Juzeliūnas, and M. Lewenstein, *Phys. Rev. Lett.* **112**, 043001 (2014).
  - [26] M. Mancini, G. Pagano, G. Cappellini, L. Livi, M. Rider, J. Catani, C. Sias, P. Zoller, M. Inguscio, M. Dalmonte, and L. Fallani, *Science* **349**, 1510 (2015).
  - [27] N. R. Cooper and A. M. Rey, *Phys. Rev. A* **92**, 021401 (2015).
  - [28] M. L. Wall, A. P. Koller, S. Li, X. Zhang, N. R. Cooper, J. Ye, and A. M. Rey, *Phys. Rev. Lett.* **116**, 035301 (2016).
  - [29] C. D. Batista and G. Ortiz, *Advances in Physics* **53**, 1 (2004).
  - [30] See the Supplementary Material, which includes Refs. [25, 26, 36–39, 48–54], for technical details of this calculation.
  - [31] P. W. Anderson, *Journal of Physics C: Solid State Physics* **3**, 2436 (1970).
  - [32] A. Georges, L. de’ Medici, and J. Mravlje, *Annual Review of Condensed Matter Physics* **4**, 137 (2013).
  - [33] In a 2D optical lattice, the hopping in an excited band generally depends on direction due to different motional states. This complication may be avoided, if uses the third excited band for mobile atoms.
  - [34] See the Supplementary Material for further details of the cold-atom implementation (5).
  - [35] See the Supplementary Material for a detailed explanation when one can ignore the doubly-occupied states, and for a calculation of second-order corrections  $\sim J_0^2/\Omega$ .
  - [36] U. Schollwöck, *Ann. Phys.* **326**, 96 (2011).
  - [37] G. Vidal, *Physical Review Letters* **93**, 040502 (2004).
  - [38] S. R. White and A. E. Feiguin, *Physical Review Letters* **93**, 076401 (2004).
  - [39] A. J. Daley, C. Kollath, U. Schollwöck, and G. Vidal, *Journal of Statistical Mechanics: Theory and Experiment* **2004**, P04005 (2004).
  - [40] See the Supplementary Material for dynamics of single-particle wavepackets.
  - [41] W. Kohn, *Phys. Rev.* **133**, A171 (1964).
  - [42] D. J. Scalapino, S. R. White, and S. Zhang, *Phys. Rev. B* **47**, 7995 (1993).
  - [43] See the Supplementary Material for details of DMRG simulations.
  - [44] See the Supplementary Material for derivation of the Drude weight  $\mathcal{D}$  for non-interacting  $d$ -fermions.
  - [45] See the Supplementary Material for a comparison of the wavepacket dynamics in these two cases.
  - [46] J. Mun, P. Medley, G. K. Campbell, L. G. Marcassa, D. E. Pritchard, and W. Ketterle, *Phys. Rev. Lett.* **99**, 150604 (2007).
  - [47] M. Raizen, C. Salomon, and Q. Niu, *Physics Today* **50**, 30 (1997).
  - [48] M. Cazalilla and A. Rey, *Reports on Progress in Physics* **77**, 124401 (2014).

- [49] B. K. Stuhl, H.-I. Lu, L. M. Aycock, D. Genkina, and I. B. Spielman, *Science* **349**, 1514 (2015).
- [50] L. Fallani, C. Fort, J. Lye, and M. Inguscio, *Opt. Express* **13**, 4303 (2005).
- [51] H. Katori, M. Takamoto, V. G. Pal'chikov, and V. D. Ovsiannikov, *Phys. Rev. Lett.* **91**, 173005 (2003).
- [52] G. K. Campbell, A. D. Ludlow, S. Blatt, J. W. Thomsen, M. J. Martin, M. H. G. de Miranda, T. Zelevinsky, M. M. Boyd, J. Ye, S. A. Diddams, T. P. Heavner, T. E. Parker, and S. R. Jefferts, *Metrologia* **45**, 539 (2008).
- [53] M. S. Safronova, Z. Zuhrianda, U. I. Safronova, and C. W. Clark, arXiv:1507.06570.
- [54] I. Gradshteyn and I. Ryzhik, *Table of Integrals, Series, and Products* (Elsevier Science, 2014).



# Supplementary material for: “Spin-orbit coupled correlated metal phase in Kondo lattices: an implementation with alkaline-earth atoms”

## DERIVATION OF THE MODEL IN EQ. (4)

The effective low-energy model (4) was obtained by projecting the full Hamiltonian (1) of a solid-state FKLM [or its AMO analog in Eq. (5)] onto the s-t subspace (3). In this section, we describe details of this derivation.

The s-t manifold (3) is spanned by the states  $|s\rangle_i = r_- a_{i\uparrow}^\dagger |\downarrow\rangle_i + r_+ a_{i\downarrow}^\dagger |\uparrow\rangle_i$  and  $|t\rangle_i = a_{i\uparrow}^\dagger |\uparrow\rangle_i$  that diagonalize *local magnetic interactions* in the Hamiltonian (1) [see discussion after Eq. (2)]. These local terms contribute a detuning from the s-t resonance

$$H_{\text{loc}} \rightarrow \Delta \sum_i [|s\rangle_i \langle s|_i - |t\rangle_i \langle t|_i].$$

Hence, we only need to compute matrix elements in the s-t subspace of the kinetic energy from Eq. (1). In the staggered frame (2), it has the form  $H_0 = -J_0 \sigma_{nm}^x \sum_{\langle ij \rangle} (a_{in}^\dagger a_{jm} + \text{h.c.})$ . Because a given lattice site can not be simultaneously occupied by a singlet and a triplet (no double occupancy constraint), non-zero matrix elements will be between states of the type  $|\alpha\rangle_i |\uparrow\rangle_j$  and  $|\uparrow\rangle_i |\beta\rangle_j$  with  $\alpha, \beta = s$  or  $t$ , and nearest-neighbor (NN) sites  $i$  and  $j$ . We have:

$$\begin{aligned} H_0 |s\rangle_i |\uparrow\rangle_j &= -J_0 [r_- a_{i\downarrow}^\dagger a_{j\uparrow}^\dagger |\uparrow\rangle_j + r_+ |\uparrow\rangle_i |t\rangle_j] \rightarrow \\ &\rightarrow -J_0 r_+ |\uparrow\rangle_i |t\rangle_j, \\ H_0 |t\rangle_i |\uparrow\rangle_j &= -J_0 |\uparrow\rangle_i a_{j\downarrow}^\dagger |\uparrow\rangle_j = \\ &= -J_0 |\uparrow\rangle_i [r_+ |s\rangle_j - r_- |t\rangle_j] \rightarrow J_0 r_+ |\uparrow\rangle_i |s\rangle_j. \end{aligned}$$

The crossed terms are off-resonant, i.e. do not belong to the local s-t manifold. Combining  $H_0$  and  $H_{\text{loc}}$ , we obtain  $H_d$ , Eq. (4), with  $J = J_0 r_+$ .

For the AEA Hamiltonian (5), the s-t subspace is defined by the local states  $|s\rangle_i = \frac{1}{\sqrt{2}} [a_{i\uparrow}^\dagger |\downarrow\rangle_i - a_{i\downarrow}^\dagger |\uparrow\rangle_i]$  and  $|t\rangle_i = a_{i\downarrow}^\dagger |\downarrow\rangle_i$ . Performing same steps as above, we arrive at the model (4) with  $J = J_0/\sqrt{2}$ .

## ALKALINE-EARTH ATOMS IN A LASER-INDUCED MAGNETIC FIELD

This section is dedicated to general remarks regarding the setup with AEAs in an optical lattice shown in Fig. 1(d) and described by Eq. (5). Among other issues, we will clarify the FM nature of atomic exchange interactions, the origin of the artificial Zeeman field  $\Omega$ , and justify our focus on the singlet-triplet resonance that played a central role in the main text.

## Exchange interactions and artificial Zeeman field

Alkaline-earth fermionic atoms, such as  $^{171}\text{Yb}$ ,  $^{173}\text{Yb}$  and  $^{87}\text{Sr}$ , have two valence electrons in a state with total angular momentum  $J_t = 0$ , and a finite nuclear spin  $I$  ( $I = 1/2, 5/2$  and  $9/2$  for  $^{171}\text{Yb}$ ,  $^{173}\text{Yb}$  and  $^{87}\text{Sr}$ , respectively) [1]. Additionally, there are two electronic “clock” states: lowest-energy orbital singlet  $^1S_0$  ( $|g\rangle$ ) and an excited triplet  $^3P_0$  ( $|e\rangle$ ). Because  $|e\rangle$  and  $|g\rangle$  configurations have  $J_t = 0$ , they are almost perfectly decoupled from the nuclear degrees of freedom during s-wave collisions, which allows us to use either electronic or nuclear-spin states to encode pseudo-spin flavors  $n = \uparrow, \downarrow$ . At the level of only s-wave two-atom interactions, both choices yield the FM form of the exchange coupling in Eq. (5).

Indeed, suppose that all atoms are nuclear spin-polarized and pseudo-spins  $n = \uparrow, \downarrow$  are identified with clock states  $|e, g\rangle$ . Since the two atoms reside in two different Bloch bands [lowest  $|1\rangle$  and excited  $|2\rangle$ , see Fig. 1(d)], we must antisymmetrize their total, i.e. spatial and electronic, wavefunction. If we focus only on s-wave two-body collisions, the spatial wavefunction must be symmetric and electronic part – antisymmetric, so only *eg*-singlets can scatter. Because the corresponding scattering length  $a_{eg}^-$  is positive, the *eg* two-body singlet has higher energy than the triplet, leading to a FM exchange  $V < 0$  (which favors *eg*-triplets with zero energy).

These arguments remain essentially unchanged in the other case when pseudo-spins  $\uparrow$  and  $\downarrow$  are associated with any two nuclear spin states. In this case, we assume that all atoms are prepared in the lowest clock configuration  $|g\rangle$ . As before, the spatial part of the wavefunction must be symmetric, so the only scattering channel is nuclear-spin singlet with a positive scattering length  $a_{gg}$ . Thus, the exchange  $V$  is again FM, and our analysis in the main text covers both above cases.

In the pseudo-spin language, the FM exchange interaction has full  $SU(2)$  symmetry, see Eq. (5). This fact is a consequence of the decoupling between electronic and nuclear-spin degrees of freedom [1], but can also be understood by recalling that only pseudo-spin *singlets* participate in s-wave collisions. The  $SU(2)$  symmetry of interactions allows us to choose the spin quantization axis arbitrarily, and simplify the artificial magnetic field term.

The latter is laser-induced by coupling internal atomic levels via direct optical (if pseudo-spins correspond to electronic *e-g* states) or Raman two-photon (when pseudo-spins are encoded in nuclear spins) transitions [2–4]. This coupling is equivalent to a magnetic field along

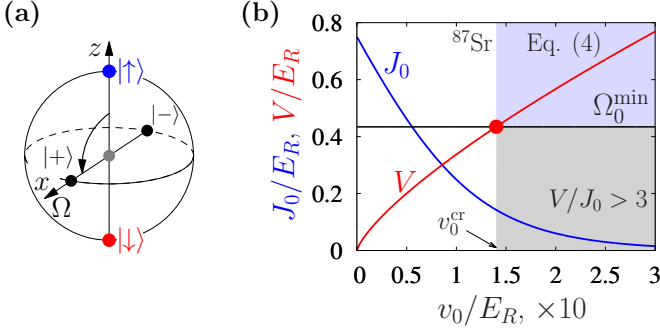


FIG. S1. (a) Rotation that aligns the  $z$ -axis in pseudo-spin space with the direction of the artificial magnetic field  $\Omega$ . (b) Excited-band hopping  $J_0$  and interband exchange interaction  $V$  in the Sr optical lattice clock as functions of the lattice depth  $v_0$ . The photon recoil energy is  $E_R \approx 3.2$  kHz. The red dot marks the lowest value of the Rabi coupling at a s-t resonance  $\Omega_0^{\text{min}} = V(v_0^{\text{cr}})$  when  $V/J_0 = 3$ . Gray shading shows the range of lattice depths with  $V/J_0 > 3$ . When in addition  $\Omega > \Omega_0^{\text{min}}$  (light blue region) the effective Hamiltonian (4) is a good approximation to the full model (5).

the  $x$ -axis:  $H_R = \Omega \sigma_{ab}^x |a\rangle\langle b|$  with  $a$  and  $b = \uparrow, \downarrow$ . We can use the  $SU(2)$  symmetry and rotate the basis to align the  $z$ -axis with this field, see Fig. S1:  $H_R = \Omega \sigma_{ab}^z |a\rangle\langle b|$ .

### Realizing a staggered artificial magnetic field

The quantum simulator AEA setup in Eq. (5) relies on a staggered nature of the laser-induced artificial magnetic field that has opposite signs on NN lattice sites. Naturally, an implementation of this  $\pi$ -modulated field depends on the physical degrees of freedom used to encode pseudo-spin flavors.

First, let us assume that pseudo-spins  $\uparrow, \downarrow$  correspond to nuclear-spin states (with all atoms in the  $|g\rangle$  electronic configuration) and are coupled via two-photon Raman transitions [3, 4] using retroreflected laser beams with wavevectors  $\mathbf{k}_1$  and  $-\mathbf{k}_2$ . In this setup, spatial dependence of the laser-induced field is given by a standing wave  $\Omega e^{i(\mathbf{k}_1 - \mathbf{k}_2) \cdot \mathbf{x}_i} + \text{c.c.}$  ( $\mathbf{x}_i$  labels optical lattice sites, and “c.c.” stands for “complex-conjugate”). In 1D,  $\mathbf{x}_i = \mathbf{e}_0 a_0 i$  with  $a_0$  being the lattice spacing and  $\mathbf{e}_0$  – a unit vector along the lattice that forms an angle  $\alpha$  with  $\mathbf{k}_1 - \mathbf{k}_2$ . One way to achieve a staggered artificial field, is to tune this angle so that  $\cos \alpha = \pi/a_0 |\mathbf{k}_1 - \mathbf{k}_2|$ . Alternatively, one can simply adjust the wavelength of the optical lattice potential  $\lambda_0 = 2a_0$  to match the wavelength of a laser that imprints the staggered phase. This can be done by tuning the relative angle  $\vartheta$  between lattice laser beams [5] as  $a_0 = \lambda_0/2 \sin \frac{\vartheta}{2}$ .

The situation is slightly different when pseudo-spin components are encoded with clock  $|e\rangle$  and  $|g\rangle$  states, because the optical lattice wavelength must be magic,

i.e. chosen in such a way that electronic polarizabilities of both electronic configurations coincide [6]. This magic wavelength,  $\lambda_0^m$ , needs to be small enough compared to the wavelength  $\lambda_c$  of the  $e$ - $g$  transition, so that the equality  $(2\pi/\lambda_c)a_0^m = \pi\lambda_0^m/\lambda_c \sin \frac{\vartheta}{2} = \pi$  or  $\sin \frac{\vartheta}{2} = \lambda_0^m/\lambda_c$  can be satisfied for some value of  $\vartheta$ . For example, for  $^{87}\text{Sr}$ ,  $\lambda_c = 698$  nm [7] and there are five magic wavelengths [8]: one at  $\lambda_0^m = 813$  nm and four with  $\lambda_0^m < \lambda_c$ . Using any of the latter for optical lattice lasers (plus a retroreflected probing beam at the resonance with the  $e$ - $g$  transition) would realize the staggered artificial magnetic field.

Another way of implementing the staggered artificial field is to load atoms in a 3D anisotropic optical lattice where tunneling along one direction exceeds hopping in the other directions. In this geometry, by aligning the clock laser w.r.t. to the relevant tunneling direction, one can ensure that it imprints a phase of  $\pi$  on the atoms.

### Estimates of experimental parameters

Having discussed general features of the proposed experimental setup, here we estimate relevant energy scales required to realize the correlated metal state in Figs. 1(c) and Fig. 3. We assume that the experiment will use  $^{87}\text{Sr}$  atoms in a magic optical lattice (wavelength  $\lambda_m$ ) described by a potential  $V_{\text{las}}(\mathbf{x}) = v_0(\sin^2 kx + \sin^2 ky + \sin^2 kz)$  with  $k = 2\pi/\lambda_m$ , and consider identical confinement along all directions.

In Fig. S1(b) we show lattice-depth ( $v_0$ ) dependence of the hopping amplitude  $J_0$  between same spatial orbitals in an excited band, and exchange interaction  $V$  between the lowest and first excited bands. The parameters of the system are: atomic mass  $m_{\text{Sr}} = 87$  a.u.; magic wavelength  $\lambda_m = 813$  nm which translates into a recoil energy  $E_R = \frac{\hbar^2 k^2}{2m_{\text{Sr}}} \approx 3.2$  kHz; and scattering length  $a = a_{gg} \sim a_{eg}^- \sim 200 a_0$  ( $a_0$  is the Bohr radius). We compute the hopping  $J_0$  by directly solving a 1D single-particle Schrödinger equation in the periodic potential  $V_{\text{las}}^{\text{1D}} = v_0 \sin^2 kx$ , as a quarter of the first excited band width. To find the interband exchange, we employ a harmonic approximation  $V_{\text{las}} \approx v_0 k^2 \mathbf{x}^2 \equiv \frac{1}{2} m_{\text{Sr}} \omega^2 \mathbf{x}^2$  with  $\omega = \frac{2}{\hbar} \sqrt{v_0 E_R}$ . Following the procedure explained in the next subsection and using the above numerical values, one obtains  $V(v_0)/E_R \approx 0.06(v_0/E_R)^{3/4}$ .

We can use these results to determine experimental conditions under which the effective low-energy model (4) is realized. First,  $V/J_0$  must be large. As we show in the last section of this Supplementary Material, Eq. (4) provides a satisfactory approximation to the full model (5) even for  $V \gtrsim 2J_0$  and small detuning  $\Omega \sim V$ . Hence, we require  $V/J_0 > 3$  [gray region in Fig. S1(b)] which puts a lower bound on the lattice depth  $v_0^{\text{cr}} = 14 E_R$ .

Next, the Rabi coupling  $\Omega$  must be close to its value  $\Omega_0 = V$  at the s-t resonance [see Figs. 1(d) and 1(e)], in the sense that even for a detuning  $\Delta \sim J_0$ , both  $V$  and  $\Omega$



remain larger than  $J_0$ . The lower bound on  $\Omega_0$  is given by  $\Omega_0^{\min} = V(v_0^{\text{tr}}) \sim 1.5 \text{ kHz}$  [black line in S1(b)]. For deeper lattices with  $v_0 > v_0^{\text{tr}}$ , the low-energy model (4) should become more accurate and offer access to a wider range of detunings  $\Delta$ , provided a strong enough  $\Omega > \Omega_0^{\min}$  can be realized [light blue region in Fig. S1(b)].

### Role of the local intraband scattering (Hubbard repulsion)

So far we assumed that the local repulsion  $U$  in Eq. (5) can be ignored. Now we will identify the parameter regime where this assumption is valid.

Let us first consider a single well and compute the energy of a state with three particles: one in the lowest and two in the higher band. There is only one relevant  $s$ -wave scattering energy,  $u_s > 0$ , that corresponds to a pseudo-spin singlet state. Depending on whether pseudo-spin degrees of freedom are implemented with electronic  $g$  and  $e$  states of nuclear-spin polarized atoms, or with nuclear spins of atoms in the  $g$  clock state,  $u_s = \frac{4\pi}{m} a_{eg}^-$  or  $\frac{4\pi}{m} a_{gg}$ , respectively (we use the units with  $\hbar = 1$ ). The single-well effective Hamiltonian (omitting the site index  $i$ ) can be written as [cf. Eq. (5)]:

$$H_{\text{ex}} = \frac{U}{2} n_2^c (n_2^c - 1) + V \left[ \sum_{\sigma} n_{1\sigma}^c n_{2,-\sigma}^c - (c_{1\uparrow}^\dagger c_{1\downarrow}^\dagger c_{2\downarrow}^\dagger c_{2\uparrow} + c_{1\downarrow}^\dagger c_{1\uparrow}^\dagger c_{2\uparrow}^\dagger c_{2\downarrow}) \right],$$

where  $n_a^c = \sum_{\sigma} c_{a\sigma}^\dagger c_{a\sigma}$ , and indices  $a = 1, 2$  denote lowest and excited bands (motional states). Because the triplet state has zero energy, this Hamiltonian adds an energy shift  $V n_2^c$  to each on-site term in  $H$  from Eq. (5).

To estimate a relative magnitude of  $U$  and  $V$ , we assume a 1D harmonic quantum well  $\mathcal{V}(x) = \frac{1}{2} m \omega^2 x^2$  where only lowest  $n = 0$  and excited  $n = 1$  states are populated. Then a simple calculation yields:

$$U = u_s^{1\text{D}} \int_{-\infty}^{\infty} dz |\phi_1(z)|^4 = \frac{3u_s^{1\text{D}}}{\sqrt{32\pi}l_0},$$

$$V = u_s^{1\text{D}} \int_{-\infty}^{\infty} dz |\phi_0(z)\phi_1(z)|^2 = \frac{u_s^{1\text{D}}}{\sqrt{8\pi}l_0},$$

where  $\phi_n(z) = h_n(z/l_0) e^{-z^2/2l_0^2} / \sqrt{2^n n! \sqrt{\pi} l_0}$ ,  $h_n(\xi)$  are Hermite polynomials [9], and  $l_0 = 1/\sqrt{m\omega}$ . The coefficient  $u_s^{1\text{D}}$  is a “projected” three-dimensional energy scale  $u_s$  that takes into account the transverse confinement:

$$u_s^{1\text{D}} = u_s \int dx dy |\phi_{\perp}(x, y)|^4,$$

$\phi_{\perp}(x, y)$  is a transverse mode that we assume to be the same for both longitudinal states  $\phi_0(z)$  and  $\phi_1(z)$ .

There are two degenerate three-particle states:  $|3, \sigma\rangle = c_{1\sigma}^\dagger c_{2\uparrow}^\dagger c_{2\downarrow}^\dagger |0\rangle$  with an energy  $U_3 = U + V = 5u_s^{1\text{D}}/\sqrt{8\pi}l_0$ .

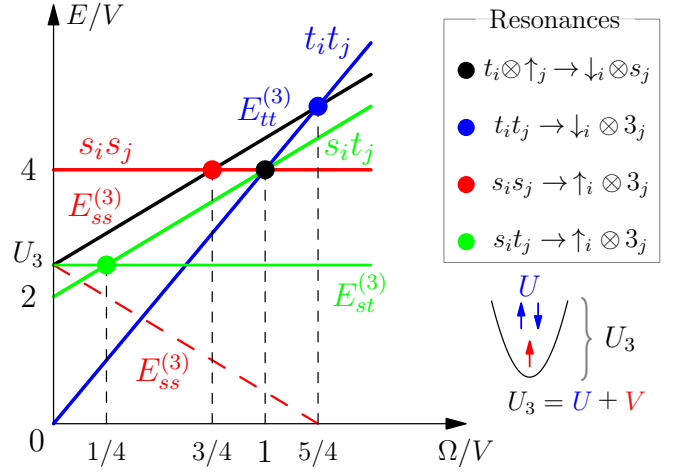


FIG. S2. Energies of the four-fermion system on two lattice sites as functions of the staggered field  $\Omega$  (see text for notations). Red, blue and green lines correspond to  $|s_i s_j\rangle$ ,  $|t_i t_j\rangle$  and  $|s_i t_j\rangle$  initial states, respectively (as indicated in the plot). Other lines of the same color are energies of the states  $|\sigma_i\rangle \otimes |3, \sigma'\rangle_j$  obtained from the initial ones after single-fermion hopping. The black line includes two energy levels:  $E_{tt}^{(3)}$  (blue) and  $E_{ss}^{(3)}$  (red). The dashed red line corresponds to  $E_{ss}^{(3)}$  which can not become resonant with other (red-colored) states at  $\Omega > 0$ . The circles mark different resonances: the singlet-triplet crossing in Fig. 1(c) is identified by the black circle; other colors denote situations when one of the states involves a doubly occupied excited band. These states are off-resonant and can be ignored as long as the system is not too far detuned from the s-t resonance (i.e.  $\Delta < V/4$ ).

We would like these states to be off-resonant, so that no hopping process could connect them to any state within the s-t subspace. Such processes can be computed by applying the excited-band hopping  $c_{2,j\sigma}^\dagger c_{2,i\sigma}$  ( $i$  and  $j$  are lattice sites) to each of the two neighboring two-particle states  $|s_i s_j\rangle$ ,  $|s_i t_j\rangle$  and  $|t_i t_j\rangle$ . We will assume that in the original (lab) frame  $\Omega_i = \Omega$ ,  $\Omega_j = -\Omega$ , and therefore  $|t_i\rangle = c_{2,i\downarrow}^\dagger |\downarrow_i\rangle$ ,  $|t_j\rangle = c_{2,j\uparrow}^\dagger |\uparrow_j\rangle$ . The resulting target states and their energies are:  $|s_i s_j\rangle \rightarrow |\downarrow_i\rangle \otimes |3, \uparrow\rangle_j + |\uparrow_i\rangle \otimes |3, \downarrow\rangle_j$  [ $E_{ss}^{(3)} = \pm 2\Omega + U_3$ , respectively],  $|s_i t_j\rangle \rightarrow |\uparrow_i\rangle \otimes |3, \uparrow\rangle_j$  [ $E_{st}^{(3)} = U_3$ ],  $|t_i t_j\rangle \rightarrow |\downarrow_i\rangle \otimes |3, \uparrow\rangle_j$  [ $E_{tt}^{(3)} = 2\Omega + U_3$ ]. In Fig. S2 we compare  $E^{(3)}$  with the sum of singlet and triplet energies. It follows that three-particle states are off-resonant if the detuning from the s-t resonance  $\Omega = V$  does not exceed  $V/4$ .

### Corrections to the effective model in Eq. (4)

The effective low-energy Hamiltonian  $H_d$  in Eq. (4) approximates the full model (5) to a leading (first) order in  $J_0/\Omega$  (or  $J_0/V$ ). Here we compute second-order corrections  $\sim J_0^2/\Omega$  that involve off-resonant states outside

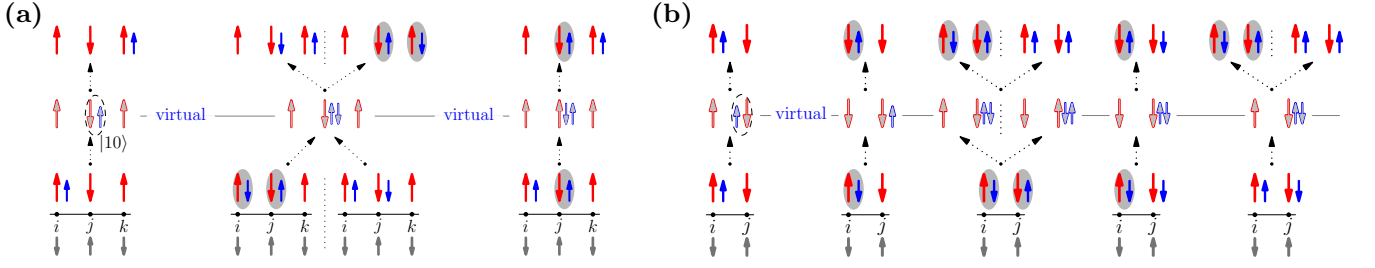


FIG. S3. Panel (a) Virtual processes leading to the next-NN correlated hopping in Eq. (S1). Red (blue) arrows correspond to spins of local (itinerant) atoms. Virtual states are indicated by empty arrows. Thick gray arrows denote the artificial magnetic field  $\Omega$ . Filled gray ellipses are spin-singlet  $|00\rangle$  states, while the dashed ellipse denotes a  $|10\rangle$  triplet. An itinerant atom is transferred from site  $i$  to  $k$  through an intermediate site  $j$ , whose state may change in the process. (b) Fluctuations that give rise to the density and exchange interactions in Eq. (S1). Notations are the same as in panel (a).

of the s-t subspace. We will assume that  $J_0$  and  $\Delta$  are small compared to  $V$  and  $\Omega$ , and hence neglect the difference  $V - \Omega$  in the energy denominators. Our analysis is generic and valid in any space dimension.

There are two types of second-order corrections: next-NN (NNN) correlated hopping, and density and exchange-like interactions. The NNN hopping involves two links (three sites) and is conditional on the state at an intermediate site [see Fig. S3(a)]. On the other hand, density and exchange-like interactions involve only pairs of sites (single link), as shown in Fig. S3(b).

We start by computing the action of a single kinetic-energy link  $l_{ij} = -J_0 \sum_n (c_{in}^\dagger c_{jn} + \text{h.c.})$  on two types of initial states:  $|\psi_{\text{in}}^1\rangle = d_{j\beta}^\dagger |\text{vac}\rangle$  and  $|\psi_{\text{in}}^2\rangle = d_{i\alpha}^\dagger d_{j\beta}^\dagger |\text{vac}\rangle$

with  $\alpha$  and  $\beta$  being either  $s$  or  $t$ . In practice, this is easier to accomplish in the staggered frame (2) when  $l_{ij} = -J_0 \sigma_{nm}^x (a_{in}^\dagger a_{jm} + \text{h.c.})$ . Energies of these states are  $E_{\text{in}}^1 = (\frac{3}{2}\Omega)_j + \Omega_i = \frac{5}{2}\Omega$  and  $E_{\text{in}}^2 = 2 \times \frac{3}{2}\Omega = 3\Omega$ . In the intermediate states  $l_{ij}|\psi_{\text{in}}^1\rangle$ , we keep only those components, orthogonal to the s-t manifold in Fig. 1(e) (marked by a red circle). We have:

$$l_{ij}|\psi_{\text{in}}^1\rangle \rightarrow \frac{J_0}{2} \delta_{\beta s} \left[ \underbrace{|00\rangle_i |\uparrow_j\rangle}_{3\Omega/2 - \Omega} + \underbrace{|10\rangle_i |\uparrow_j\rangle}_{-\Omega/2 - \Omega} \right] - \frac{J_0}{\sqrt{2}} \delta_{\beta t} \underbrace{|10\rangle_i |\downarrow_j\rangle}_{-\Omega/2 + \Omega}$$

and for the state  $|\psi_{\text{in}}^2\rangle$

$$\begin{aligned} l_{ij}|\psi_{\text{in}}^2\rangle \rightarrow & \frac{J_0}{2} \delta_{\alpha s} \delta_{\beta s} \underbrace{(a_{i\uparrow}^\dagger a_{i\downarrow}^\dagger - a_{j\uparrow}^\dagger a_{j\downarrow}^\dagger) |\uparrow_i \uparrow_j\rangle}_{U - 2\Omega} + J_0 \left[ \delta_{\alpha t} \delta_{\beta t} - \frac{1}{2} \delta_{\alpha s} \delta_{\beta s} \right] \underbrace{(a_{i\uparrow}^\dagger a_{i\downarrow}^\dagger - a_{j\uparrow}^\dagger a_{j\downarrow}^\dagger) |\downarrow_i \downarrow_j\rangle}_{U + 2\Omega} - \\ & - \frac{J_0}{\sqrt{2}} \underbrace{(a_{i\uparrow}^\dagger a_{i\downarrow}^\dagger - a_{j\uparrow}^\dagger a_{j\downarrow}^\dagger) [\delta_{\alpha s} \delta_{\beta t} |\uparrow_i \downarrow_j\rangle + \delta_{\alpha t} \delta_{\beta t} |\downarrow_i \uparrow_j\rangle]}_U, \end{aligned}$$

where energies of the intermediate states are shown as blue under-scripts. Applying the link operators to the

right-hand sides of these expressions, we arrive at a second-order correction to the effective model in Eq. (4)

$$\begin{aligned} H_{\text{ef}}^{(2)} = & \frac{J_0^2}{4\Omega} \sum_{\Delta(ijk)} (1 - n_i^d) (d_{kt}^\dagger d_{js} + \text{h.c.}) + \frac{J_0^2}{4\Omega} \sum_{\langle ij \rangle} \left[ (1 - n_i^d) n_{jt}^d + \frac{3}{4} (1 - n_i^d) n_{js}^d + (i \leftrightarrow j) \right] + \\ & + \frac{J_0^2}{\Omega - U} \sum_{\langle ij \rangle} \left[ \frac{3\Omega - U}{5\Omega - U} n_{is}^d n_{js}^d + 2 n_{it}^d n_{jt}^d + \frac{\Omega - U}{3\Omega - U} (n_{is}^d n_{jt}^d + n_{it}^d n_{js}^d) - (d_{is}^\dagger d_{js}^\dagger d_{jt} d_{it} + d_{it}^\dagger d_{jt}^\dagger d_{js} d_{is}) \right] - \\ & - \frac{J_0^2}{\Omega - U} \sum_{\Delta(ijk)} \left[ d_{kt}^\dagger d_{it}^\dagger d_{is} d_{js} + d_{ks}^\dagger d_{is}^\dagger d_{it} d_{jt} - \frac{1}{2} d_{ks}^\dagger n_{is}^d d_{js} - 2 d_{kt}^\dagger n_{it}^d d_{jt} - \frac{\Omega - U}{3\Omega - U} d_{kt}^\dagger n_{is}^d d_{jt} + (i \leftrightarrow j) + \text{h.c.} \right]. \end{aligned} \quad (\text{S1})$$

The 1st [2nd and 3rd] line corresponds to  $|\psi_{\text{in}}^1\rangle$  [ $|\psi_{\text{in}}^2\rangle$ ], and

$\sum_{\Delta(ijk)}$  denotes summation over all triples of sites  $i, j$

and  $k$ . In 1D it corresponds to second-nearest neighbors, while in 2D – to second- and third-nearest neighbors.

### WAVEPACKET DYNAMICS WITH NON-INTERACTING FERMIONS IN 1D

In the main text we presented evolution of many-body wavepackets that can be determined only numerically. Here we illustrate hallmark properties of the model (4), such as emergence of the transverse local magnetic polarization, by studying the case of canonical (i.e. non-interacting)  $d$ -fermions when Eq. (4) is the complete Hamiltonian of the system and the Schrodinger equation can be solved analytically for any initial condition.

We can straightforwardly diagonalize the Hamiltonian (4) by rewriting it in the momentum space:

$$H = \sum_k d_k^\dagger [-2J \cos k \sigma^x + \Delta \sigma^z] d_k.$$

For a fixed momentum  $k$ , there are two quasiparticle states  $f_{k,\pm}$  with energies  $\varepsilon_{k,\pm} = \pm \rho_k$ ,  $\rho_k = \sqrt{(2J \cos k)^2 + \Delta^2}$  shown in the left panel in Fig. S4. The  $d$ -operators can be written as:

$$\begin{pmatrix} d_{ks} \\ d_{kt} \end{pmatrix} = \begin{pmatrix} \cos \frac{\vartheta_k}{2} f_{k,+} - \sin \frac{\vartheta_k}{2} f_{k,-} \\ \sin \frac{\vartheta_k}{2} f_{k,+} + \cos \frac{\vartheta_k}{2} f_{k,-} \end{pmatrix} = \begin{pmatrix} \sum_\lambda V_k^\lambda f_{k\lambda} \\ \sum_\lambda U_k^\lambda f_{k\lambda} \end{pmatrix} \quad (\text{S2})$$

with  $\tan \vartheta_k = -2J \cos k / \Delta$  and  $\lambda = \pm$ .

#### Single-fermion case

Let us first consider a situation with only one fermion, whose wavefunction at  $t = 0$  is a fully polarized (triplet) Gaussian wavepacket centered at  $x_i = x_0$ , with a width  $\sigma$  and momentum  $k_0$ :

$$|\psi_0\rangle = A \sum_i e^{-(x_i - x_0)^2 / 2\sigma^2} e^{ik_0 x_i} d_{it}^\dagger |\text{vac}\rangle.$$

This state is normalized as  $\langle \psi_0 | \psi_0 \rangle = 1$  ( $A$  is the normalization constant). The time-dependent solution can be readily written as:

$$|\psi(t)\rangle = \sum_k \beta(k) \left( \sin \frac{\vartheta_k}{2} e^{-i\varepsilon_{k,+}t} f_{k,+}^\dagger + \cos \frac{\vartheta_k}{2} e^{-i\varepsilon_{k,-}t} f_{k,-}^\dagger \right) |\text{vac}\rangle,$$

where  $\beta(k)$  is a Fourier transform of the original packet

$$\beta(k) = \frac{A}{\sqrt{N}} \sum_i e^{-(x_i - x_0)^2 / 2\sigma^2} e^{i(k_0 - k)x_i}. \quad (\text{S3})$$

We are interested in the time-dependent local spin-resolved density  $n_{i\alpha}^d(t) = \langle \psi(t) | d_{i\alpha}^\dagger d_{i\alpha} | \psi(t) \rangle$  (no summation over  $\alpha$ ) and transverse spin polarization  $T_i^x(t) =$

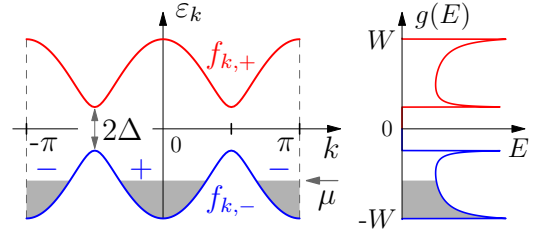


FIG. S4. Band structure of quasiparticles in Eq. (S2) (left) and their density of states (S5) (right).  $W = \sqrt{(2J)^2 + \Delta^2}$  was defined in Fig. 3. Gray shading indicates the filled Fermi sea;  $\mu$  is the corresponding chemical potential.

$-\frac{1}{\sqrt{8}} \sigma_{\alpha\beta}^x \langle \psi(t) | d_{i\alpha}^\dagger d_{i\beta} | \psi(t) \rangle$ . Using the relation  $d_{i\alpha}^\dagger d_{i\beta} = \frac{1}{N} \sum_{p'p} e^{i(p-p')x_i} d_{p'\alpha}^\dagger d_{p\beta}$ , one can show that  $n_{i\alpha}^d(t) = |C_{i\alpha}(t)|^2$  and  $T_i^x(t) = -\frac{1}{\sqrt{8}} C_{i\alpha}^*(t) \sigma_{\alpha\beta}^x C_{i\beta}(t)$  with

$$\begin{pmatrix} C_{is} \\ C_{it} \end{pmatrix} = \frac{1}{\sqrt{N}} \sum_k \beta(k) e^{ikx_i} \begin{pmatrix} i \frac{2J \cos k}{\rho_k} \sin \rho_k t \\ \cos \rho_k t + i \frac{\Delta}{\rho_k} \sin \rho_k t \end{pmatrix} \quad (\text{S4})$$

$C_{i\alpha}$  is a single-particle real-space wavefunction.

Due to the presence of negative energies  $\varepsilon_{k,-}$ , the initial wavepacket splits into two counter-propagating, right and left moving parts (mathematically this happens because the time dependence enters only via  $\cos \rho_k t$  and  $\sin \rho_k t$ ). Indeed, assuming that  $\beta(k)$  is peaked near the initial momentum  $k_0$  with a width  $\Delta k$ , we can approximately compute the above sums:

$$\begin{aligned} C_{it} &\sim \int_{k_0 - \Delta k}^{k_0 + \Delta k} dk \beta(k) e^{ik_0 x_i} \sum_{\lambda=\pm} \frac{\rho_k + \lambda \Delta}{2\rho_k} e^{i\lambda \rho_k t} \approx \\ &\approx \int_{-\Delta k}^{\Delta k} dk \beta(k + k_0) e^{i(k+k_0)x_i} \sum_{\lambda=\pm} \frac{\rho_{k_0} + \lambda \Delta}{2\rho_{k_0}} e^{i\lambda \rho_{k_0} t}. \end{aligned}$$

Introducing the group velocity  $v_{k_0} = -\partial \rho_k / \partial k_0$ , we have:  $C_{it} \approx \sum_\lambda [1 + \frac{\lambda \Delta}{\rho_{k_0}}] w_t(x_i - \lambda v_{k_0} t) = r_t(x_i - v_{k_0} t) + l_t(x_i + v_{k_0} t)$ , where  $w_t(\xi)$  is defined by the initial state and the two terms correspond to right and left movers (for  $v_{k_0} > 0$ ). A similar manipulation for  $C_{is}$  yields:  $C_{is} \approx \frac{J}{\rho_{k_0}} \cos k_0 \sum_\lambda w_s(x_i - \lambda v_{k_0} t)$ . In general for  $\Delta \neq 0$ ,  $|l_t| < |r_t|$  (for the same value of their arguments) and the two wavepackets are not symmetric. However, exactly at the s-t resonance  $\Delta = 0$ ,  $l_t = r_t$ , so left and right movers are mirror images of each other. For singlets,  $r_s = -l_s$ . This phase difference leads to an opposite sign of transverse local magnetization  $\langle T_i^x(t) \rangle$  for left and right moving parts of the distribution.

#### Many-particle wavepackets

The results obtained for a single  $d$ -fermion allow us to investigate wavepacket dynamics with several particles.

Specifically, we focus on the five-fermion case considered in the main text and derive a closed expression for the wavefunction and evolution of the total density.

We assume that the initial wavefunction contains only triplets, and is a ground state (GS) in a harmonic trap  $V(x_i) = A(x_i - \frac{N}{2})^2$  imposed on a chain with open boundary conditions ( $x_i = i = 0 \dots N - 1$ ):

$$|\psi_{N_d}^{\{n\}}(t=0)\rangle = \prod_{\nu} d_{n_{\nu}t}^{\dagger} |\text{vac}\rangle = \sum_{\{i\}} e^{ik_0 \sum_{\nu} x_{i_{\nu}}} \times \\ \times \prod_{\nu} \phi_{n_{\nu}}(x_{i_{\nu}}) d_{i_{\nu}t}^{\dagger} |\text{vac}\rangle = \sum_{\{k\}} \prod_{\nu} \beta_{n_{\nu}}(k_{\nu}) d_{k_{\nu}t}^{\dagger} |\text{vac}\rangle,$$

where  $\phi_n(x_i)$ ,  $n = 0, 1, \dots$  are single-particle eigenfunctions in the trap [ $\phi_n(-1) = \phi_n(N) = 0$ ] and  $\beta_n(k)$  is the Fourier transform of  $\phi_n(x)e^{ik_0x}$  defined in Eq. (S3) for a single mode. The total number of fermions is  $N_d$ ,  $\nu = 1 \dots N_d$  and  $k_0$  is the center of mass momentum. Finally,  $\{a\} = a_1 \dots a_{N_d}$  with  $a = i, n$ , etc.

At time  $t = 0$ , the trap is removed and the wavepacket starts to propagate. The time-dependent wavefunction  $|\psi_{N_d}^{\{n\}}(t)\rangle$  can be written using  $f$ -quasiparticles (S2):

$$|\psi_{N_d}^{\{n\}}(t)\rangle = \sum_{\{k\lambda\}} \prod_{\nu} \beta_{n_{\nu}}(k_{\nu}) U_{k_{\nu}}^{\lambda_{\nu}} e^{-i\epsilon_{k_{\nu}\lambda_{\nu}} t} f_{k_{\nu}\lambda_{\nu}}^{\dagger} |\text{vac}\rangle.$$

A straightforward calculation yields the position- and time-dependent total density:

$$\langle n_i^d(t) \rangle = \langle \psi_{N_d}^{\{n\}}(t) | d_{i\alpha}^{\dagger} d_{i\alpha} | \psi_{N_d}^{\{n\}}(t) \rangle = \sum_{\nu\alpha} |C_{i\alpha}^{n_{\nu}}(t)|^2,$$

where  $C_{i\alpha}^{n_{\nu}}(t)$  is a multi-mode generalization of  $C_{i\alpha}$  in Eq. (S4), with  $\beta_k \rightarrow \beta_{n_{\nu}}(k)$ .  $\langle n_{i_0}^d(t) \rangle$  is plotted in the inset of Fig. 2.

### DRUDE WEIGHT OF NON-INTERACTING $d$ -FERMIONS

Although we are interested in metallic properties of the strongly-correlated model (4), it is nevertheless instructive to study its non-interacting limit (relevant for the low-density regime), i.e. treat  $d_{i\alpha}$  as unconstrained, canonical fermions, and compute properties of this model such as the GS energy and Drude weight  $\mathcal{D}$  (as functions of the chemical potential  $\mu$ ), and the density of states.

The  $d$ -fermions on a ring pierced by a flux are described by a Hamiltonian (we call it  $H_0$  instead of  $H_d$  to emphasize lack of correlations):

$$H_0(\phi) = \sum_i [-J\sigma_{\alpha\beta}^x (d_{i\alpha}^{\dagger} e^{i\phi} d_{i+1,\beta} + \text{h.c.}) + \\ + \Delta\sigma_{\alpha\beta}^z d_{i\alpha}^{\dagger} d_{i\beta}] = \sum_k [\epsilon_k(\phi)\sigma^x + \Delta\sigma^z]_{\alpha\beta} d_{k\alpha}^{\dagger} d_{k\beta},$$

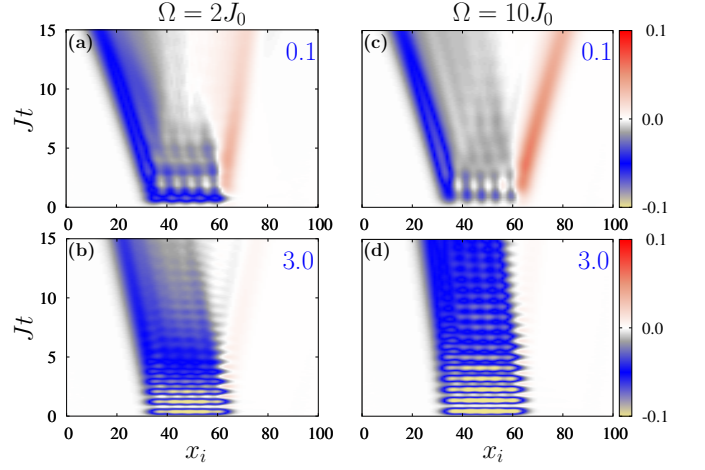


FIG. S5. Dynamics of many-body wavepackets with the same parameters as in Fig. 2, but computed within the full AEA Hamiltonian (5). Shown is the evolution of the transverse spin polarization  $\langle T_i^x \rangle$ . Panels (a) and (b) [(c) and (d)] correspond to Rabi frequency  $\Omega = 2J_0$  ( $\Omega = 10J_0$ ). The detuning  $\Delta$  is chosen to match Fig. 2:  $\Delta = 0.1J$  [(a) and (c)], and  $\Delta = 3J$  [(b) and (d)] with  $J = J_0/\sqrt{2}$ .

with  $\epsilon_k(\phi) = -2J \cos(k + \phi)$ . Its GS energy  $\mathcal{E}_0(\phi)$  is

$$\frac{\mathcal{E}_0(\phi)}{N} = \frac{1}{N} \sum_k [\epsilon_k(\phi) \sin \vartheta_k + \Delta \cos \vartheta_k] (n_{k,+}^f - n_{k,-}^f),$$

where  $n_{k\lambda}^f = \theta(\mu - \epsilon_{k\lambda})$  is the zero-temperature Fermi function. The momentum integral in this expression is trivially computed and we have

$$\frac{\mathcal{E}_0(\phi=0)}{N} = -\frac{2W}{\pi} E\left(\arcsin \frac{\sqrt{W^2 - \mu^2}}{2J}, \frac{2J}{W}\right), \\ \mathcal{D} = \frac{1}{N} \frac{\partial^2 \mathcal{E}_0}{\partial \phi^2} \Big|_{\phi=0} = \frac{4J}{\pi} E\left(\arcsin \frac{\sqrt{W^2 - \mu^2}}{W}, \frac{W}{2J}\right).$$

Here  $E(a, m) = \int_0^{\sin a} dx \sqrt{1 - m^2 x^2} / \sqrt{1 - x^2}$  is an incomplete elliptical integral of the second kind [9], and  $W = \sqrt{(2J)^2 + \Delta^2}$ . These functions are shown in the inset of Fig. 3(a).

Finally, the spin-resolved density of states of the  $f$ -quasiparticles, plotted in the right panel of Fig. S4, is

$$g(E) = \frac{1}{N} \sum_{k\lambda} \delta(E - \epsilon_{k\lambda}) = \\ = \frac{2|E| \theta(|E| - \Delta) \theta(W - |E|)}{\pi \sqrt{(E^2 - \Delta^2)(W^2 - E^2)}}. \quad (\text{S5})$$

### DETAILS OF NUMERICAL CALCULATIONS

To obtain results in the main text we performed unbiased DMRG calculations for the effective model (4).

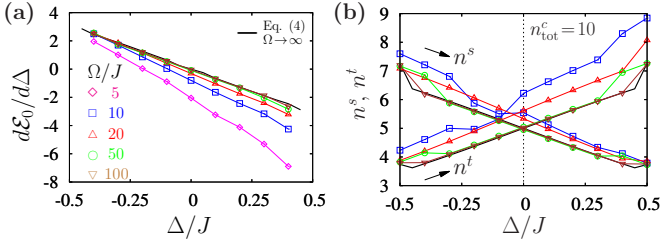


FIG. S6. GS observables within the full Hamiltonian (5) and the effective model (4). The system size is  $N = 30$  with box boundary conditions, and the chemical potential is  $\mu = -J$ . (a) Derivative of the GS energy w.r.t.  $\Delta$  for increasing  $\Omega/J$ : 5 (magenta diamonds), 10 (blue squares), 20 (red triangles), 50 (green circles), and 100 (brown inverted triangles). Solid black line is computed with the effective model (4). (b) The number of effective singlets ( $n^s$ ) and triplets ( $n^t$ ). The total number of mobile atoms is  $n_{\text{tot}}^c = \sum_{in} n_{i2n}^c = 10$ . Other notations are the same as in panel (a).

In our DMRG computations quantum states are represented by matrix product states (MPS) [10] with a particular “bond-dimension”  $D$ . In the limit of large  $D$ , this state representation becomes exact.

To compute GS properties we write the Hamiltonian as a matrix product operator (MPO) and apply a variational GS search that uses updates on neighboring sites simultaneously [10]. Periodic boundary conditions are implemented via long-range hopping terms in the MPO. Since those terms significantly increase correlations over the length of the chain, periodic boundary conditions make the calculations significantly more challenging and require larger values of  $D$ . In practice, the three-dimensional local Hilbert space of the effective model (4) allows us to scan parameter regime for a system of  $N = 40$  sites within reasonable CPU times. The local Hilbert space dimension of the full model (5) is 8, and requires significantly longer CPU times. For the GS phase diagram in Fig. 3 we use up to  $D = 265$  and find that the results are typically well converged for  $D = 128$ . The convergence is reached when relative change in energy is less than  $10^{-8}$ , with the corresponding maximum truncated weights for two-site updates are  $\sim 10^{-7}$ .

For the time-evolution calculations we use a time-dependent block decimation algorithm [11–13], which approximates an application of the time-evolution operator by a 4th order Trotter decomposition. For the many-body wave-packet dynamics in Fig. 2, the results are well converged for bond dimension  $D = 128$ .

#### Validity of effective model in Eq. (4)

In the main text, numerical calculations focused on the effective Dirac-like model (4). Here we verify its validity for the GS calculations in Fig. 3.

We compare GS observables obtained within DMRG for the effective model (4) and the full AEA model (5), which is expected to reduce to Eq. (4) in the limit of large  $\Omega$  and small  $\Delta \lesssim J$ , in a system of  $N = 30$  sites with box boundary conditions. To converge to a sector with the same number of particles we add a chemical potential term  $[\frac{1}{2}(V + \Delta) + \mu] \sum_i (n_{i2\uparrow}^c + n_{i2\downarrow}^c)$  to Eq. (5) and compute GS properties for  $\mu = -J$  and  $-\frac{1}{2} \leq \Delta/J \leq \frac{1}{2}$ .

In Fig. S6 we present a direct comparison of the GS energy derivative  $dE_0/d\Delta$  [panel (a)], and the number of local singlets  $n^s = \sum_i |s\rangle_i \langle s|_i$  with  $|s\rangle_i = \frac{1}{\sqrt{2}}[a_{i\uparrow}^\dagger |\downarrow\rangle_i - a_{i\downarrow}^\dagger |\uparrow\rangle_i]$  and triplets  $n^t = \sum_i |t\rangle_i \langle t|_i$  with  $|t\rangle_i = a_{i\downarrow}^\dagger |\downarrow\rangle_i$  [cf. Eq. (3)] in the system [panel (b)]. Clearly in the limit of large  $\Omega$  the results converge to the ones obtained within the effective model (4). Moreover, Fig. S6(b) demonstrates that for increasing  $\Omega$  the population in states outside the s-t manifold vanishes. Indeed, for the parameters of the figure the total number of particles is fixed,  $n^a = 10$ , and for large  $\Omega$  all of them belong to the s-t subspace. All these results confirm that the physics of the problem is captured by the low-energy model (4) in the strong-coupling regime  $V \sim \Omega \gg J_0$ .

#### Wave-packet dynamics in the full AEA model

For the wave-packet dynamics calculations in Fig. 2 we used the effective model (4). Here we demonstrate numerically that characteristic features of this dynamics are also present in the full AEA Hamiltonian (5), and can be observed in realistic experiments.

We use the same initial state as the one described in the main text, i.e. a wavepacket that consists of five triplets, and is produced by introducing a harmonic trapping potential and computing the ground state of the system. At time  $t = 0$ , the trap is removed and the wavepacket is accelerated by applying a phase-gradient operator. The interband exchange interaction, as well as the Hubbard repulsion are set by the detuning and Rabi frequency:  $V = \Delta + \Omega$  and  $U = 3V/2$ , respectively (see previous section). Fig. S5 shows the transverse spin polarization  $\langle T_i^x \rangle$  and demonstrates that for large  $\Omega = 10J_0$  the exact dynamics of the Dirac-like Hamiltonian (4) of Fig. 2 is reproduced. For small  $\Omega$  the effective model starts to break down, but remarkably even for  $\Omega = 2J_0$ , the full time evolution still features the characteristic splitting into two counter-propagating parts with opposite  $\langle T_i^x \rangle$  polarization for small  $\Delta < J, J_0$ .

- 
- [1] M. Cazalilla and A. Rey, Reports on Progress in Physics **77**, 124401 (2014).
  - [2] A. Celi, P. Massignan, J. Ruseckas, N. Goldman, I. B.



- Spielman, G. Juzeliūnas, and M. Lewenstein, Phys. Rev. Lett. **112**, 043001 (2014).
- [3] M. Mancini, G. Pagano, G. Cappellini, L. Livi, M. Rider, J. Catani, C. Sias, P. Zoller, M. Inguscio, M. Dalmonte, and L. Fallani, Science **349**, 1510 (2015).
- [4] B. K. Stuhl, H.-I. Lu, L. M. Aycock, D. Genkina, and I. B. Spielman, Science **349**, 1514 (2015).
- [5] L. Fallani, C. Fort, J. Lye, and M. Inguscio, Opt. Express **13**, 4303 (2005).
- [6] H. Katori, M. Takamoto, V. G. Pal'chikov, and V. D. Ovsiannikov, Phys. Rev. Lett. **91**, 173005 (2003).
- [7] G. K. Campbell, A. D. Ludlow, S. Blatt, J. W. Thomsen, M. J. Martin, M. H. G. de Miranda, T. Zelevinsky, M. M. Boyd, J. Ye, S. A. Diddams, T. P. Heavner, T. E. Parker, and S. R. Jefferts, Metrologia **45**, 539 (2008).
- [8] M. S. Safronova, Z. Zuhrianda, U. I. Safronova, and C. W. Clark, arXiv:1507.06570.
- [9] I. Gradshteyn and I. Ryzhik, *Table of Integrals, Series, and Products* (Elsevier Science, 2014).
- [10] U. Schollwöck, Ann. Phys. **326**, 96 (2011).
- [11] G. Vidal, Physical Review Letters **93**, 040502 (2004).
- [12] S. R. White and A. E. Feiguin, Physical Review Letters **93**, 076401 (2004).
- [13] A. J. Daley, C. Kollath, U. Schollwöck, and G. Vidal, Journal of Statistical Mechanics: Theory and Experiment **2004**, P04005 (2004).